

# A Latent Representation Learning Framework for Hyperspectral Image Emulation in Remote Sensing

Chedly Ben Azizi, Claire Guilloteau, Gilles Roussel, and Matthieu Puigt\*

*This work has been submitted to the IEEE for possible publication. Copyright may be transferred without notice, after which this version may no longer be accessible.*

## Abstract

Synthetic hyperspectral image (HSI) generation is essential for large-scale simulation, algorithm development, and mission design, yet traditional radiative transfer models remain computationally expensive and often limited to spectrum-level outputs. In this work, we propose a latent representation-based framework for hyperspectral emulation that learns a latent generative representation of hyperspectral data. The proposed approach supports both spectrum-level and spatial-spectral emulation and can be trained either in a direct one-step formulation or in a two-step strategy that couples variational autoencoder (VAE) pre-training with parameter-to-latent interpolation. Experiments on PROSAIL-simulated vegetation data and Sentinel-3 OLCI imagery demonstrate that the method outperforms classical regression-based emulators in reconstruction accuracy, spectral fidelity, and robustness to real-world spatial variability. We further show that emulated HSIs preserve performance in downstream biophysical parameter retrieval, highlighting the practical relevance of emulated data for remote sensing applications.

**Keywords**—hyperspectral imaging, emulation, remote sensing, variational autoencoder, deep learning, radiative transfer model, vegetation, ocean colour.

---

\*The authors are with Univ. Littoral Côte d’Opale, LISIC – UR 4491, 62219 Longuenesse, France. E-mail: [firstname.lastname@univ-littoral.fr](mailto:firstname.lastname@univ-littoral.fr).

## 1 Introduction

Hyperspectral (HS) remote sensing has become an important tool for Earth observation, providing granular insights into environmental processes and land surface characteristics. Hyperspectral imaging acquires dense spectral information across hundreds of contiguous bands for every pixel, yielding a three-dimensional data cube (two spatial dimensions and one spectral dimension) with high spectral resolution. Such data are referred to as hyperspectral images (HSI) and support a wide variety of applications, including vegetation trait retrieval, mineral and soil mapping, water quality and ocean color monitoring [1, 2]. While collections of high-quality data are continuously produced, their acquisition is often constrained by high costs, atmospheric variability, and limited spatiotemporal coverage. As a result, realistic HSI generation is essential for tasks such as algorithm development and mission design. To this end, simulation-based approaches have been developed to synthetically generate hyperspectral data under controlled conditions. In vegetation remote sensing, radiative transfer models (RTMs), such as the PROSAIL model [3], combine the PROSPECT leaf optical properties model [4] and the SAIL canopy bidirectional reflectance model [5] to simulate top-of-canopy reflectance from plant and soil bio-optical parameters. However, modeling complex non-linear physics through such numerical simulations is computationally expensive, limiting their use in large-scale generation, iterative inversion and operational scenarios. The recent development of statistical and machine learning techniques has renewed interest in emulation as a framework for synthetic data generation. Emulation involves learning surrogate models

that approximate complex simulations with a high degree of accuracy while significantly reducing computational cost. Such approaches are well established in other scientific fields, including astrophysics [6] and climate modeling [7].

In hyperspectral imaging, existing emulation approaches include classical regression-based methods based on linear dimensionality reduction, as well as more recent deep-learning-based surrogates for radiative transfer and atmospheric models, which are discussed in detail in Sect. 2. Across these approaches, most existing emulators are formulated as parameter-to-spectrum or parameter-to-band regression models. These formulations typically produce a single deterministic output per parameter configuration and do not model the underlying data distribution of hyperspectral observations. Despite the widespread use of generative deep learning for hyperspectral image analysis, parameter-conditioned generative modeling for hyperspectral image emulation remains comparatively unexplored. Recent advances in deep generative models for emulation in other scientific fields motivate the investigation of variational autoencoder-based formulations for efficient hyperspectral image emulation.

Capitalizing on the proof of concept introduced in [8], the contributions of the present work are summarized as follows:

1. We formulate hyperspectral emulation as a parameter-conditioned generative modeling problem based on variational autoencoders, providing a non-linear alternative to classical emulation approaches.
2. We propose a latent representation-based framework, using VAE as a base implementation, that supports both spectrum-level and image-level hyperspectral emulation.
3. We investigate two training formulations for parameter-conditioned emulation: a one-step approach that directly maps input parameters to hyperspectral data, and two-step approach that couples latent representation learning with parameter-to-latent space interpolation.
4. We evaluate the proposed framework on both simulated and real-world hyperspectral datasets,

and compare it against classical hyperspectral emulation methods.

The remainder of the paper is organized as follows. Section 2 reviews related work. Section 3 describes the proposed methodology. Section 4 reports the experimental setup and results, and Section 5 discusses a practical use case for hyperspectral image emulation.

## 2 Related work

### 2.1 Classical radiative transfer model emulation

Radiative transfer model (RTM) emulation has been extensively investigated in hyperspectral remote sensing, particularly in the context of vegetation spectroscopy [9]. A representative line of work is presented by Verrelst *et al.* [10–12], who developed several emulators to approximate complex RTMs for tasks such as reflectance or radiance spectra generation, interpolation and extrapolation. These approaches aim to replace computationally expensive numerical simulations with fast surrogate models conditioned on biophysical parameters.

In [10], an emulator of the SCOPE RTM model was proposed to generate synthetic canopy reflectance and sun-induced fluorescence spectra. The method follows a two-step strategy: first, a PCA is applied to simulated spectra to reduce dimensionality, then, a regression model is trained to predict the corresponding principal component coefficients from input biophysical parameters. New spectra are then reconstructed from the predicted components. Similar PCA-based emulation strategies were later applied to the emulation of spectral fitting method-based sun-induced fluorescence from HyPlant radiance data [11], and to the interpolation and extrapolation of empirical surface reflectance spectra acquired by CHRIS and HyMap sensors [12].

These classical emulation approaches have demonstrated that parameter-conditioned emulators can effectively approximate RTMs at a fraction of the computational cost. However, they are primarily designed for spectrum-level emulation and rely on linear dimensionality reduction techniques, such as PCA. While

effective for compression, these linear projections remain limited in capturing the intrinsically nonlinear relationships induced by radiative transfer physics [13]. Additionally, the methods do not explicitly account for spatial context and are therefore limited in modeling complex spatial-spectral structures inherent to hyperspectral images.

## 2.2 Deep learning-based emulators for radiative transfer and atmospheric models

Beyond classical regression-based emulation, recent studies have explored the use of deep learning models as parameter-conditioned regression surrogates for radiative transfer and atmospheric models. In [14], deep Bayesian neural networks were investigated for the emulation of the MAIAC atmospheric correction model. The authors showed that deep learning can capture complex model behavior while significantly reducing execution time compared to traditional lookup-table (LUT) interpolation. Similarly, Ojaghi *et al.* [15] introduced a one-dimensional convolutional neural network (1D-CNN) to emulate the PROSAIL and 6S radiative transfer models for efficient Bidirectional Reflectance distribution function (BRDF) modeling over Sentinel-3 OLCI spectral bands. More recently, Jasso *et al.* [16] compared different deep learning-based architectures, including multilayer perceptrons (MLPs), numerically embedded MLPs, 1D-CNNs and vision transformers, for the emulation of atmospheric correction from synthetic data generated with the 6S radiative transfer model.

These deep learning-based emulators demonstrate improved accuracy and computational efficiency over classical interpolation and regression techniques, highlighting the ability of neural networks to approximate complex forward models. Nonetheless, they are formulated as direct regression mappings from input parameters to spectral outputs, without explicitly learning a generative latent representation of hyperspectral data. As a result, they are applied at the spectrum or band level and are not designed to generate spatially coherent hyperspectral images.

## 2.3 Generative models in hyperspectral remote sensing

While generative models have been largely absent from hyperspectral image emulation, they have been widely investigated in hyperspectral remote sensing for a variety of tasks. In particular, deep generative networks have been employed for data augmentation, classification, spectral unmixing, and spectral variability modeling. This line of research demonstrates the ability of generative models to capture complex hyperspectral data distributions. Generative adversarial networks (GANs) have been proposed for data augmentation in support of hyperspectral image classification [17], as well as for hyperspectral image generation with controllable spectral variability [18] or hyperspectral image super-resolution [19]. Variational autoencoders (VAEs) have also been explored for hyperspectral data analysis, including spectral unmixing [20], and end-member library augmentation [21].

Although these generative models show strong potential for hyperspectral data generation and analysis, they are formulated for inverse or data-driven tasks, in which generation is conditioned on observed spectra, image content or labels rather than on physical or biophysical parameters. Consequently, the use of generative models for hyperspectral image emulation conditioned on physical parameters remains largely unexplored.

## 2.4 Deep generative models for emulation beyond remote sensing

Classical and deep learning-based emulators have demonstrated that surrogate models can effectively approximate complex radiative transfer and atmospheric models at a significantly reduced computational cost. In parallel, deep generative networks have shown strong potential as surrogate models for complex physical simulations and have been successfully applied to emulation tasks in other scientific domains, such as astrophysics [6].

## 2.5 Positioning of the present work

The review above highlights three complementary research directions: classical radiative transfer model emulation based on regression and dimensionality reduction, deep learning-based emulators formulated as direct regression surrogates, and deep generative models applied to hyperspectral data analysis. In addition, generative models have demonstrated their ability to act as efficient surrogates for complex physical simulations in other scientific fields.

In this work, we position hyperspectral emulation as a parameter-conditioned generative modeling problem. We propose a variational autoencoder-based framework that supports both direct parameter-to-spectra regression and latent-space generative modeling, and that can be instantiated at the spectral level as well as extended to spatial-spectral hyperspectral emulation. This formulation motivates the methodology presented in the following section.

## 3 Methodology

Building on the identified gap in the use of deep generative networks for hyperspectral emulation, we propose a VAE-based framework designed to generate hyperspectral data from associated biophysical parameters.

### 3.1 Brief background

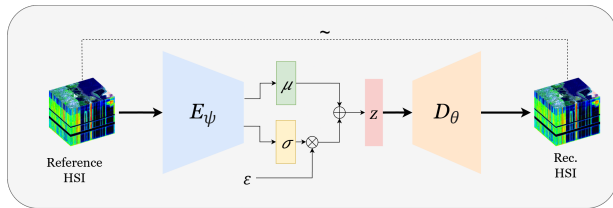


Figure 1: Overall architecture of a variational autoencoder.

**Variational autoencoder** A VAE is a generative model composed of two parts: an encoder ( $E_\psi$ ) that approximates the posterior  $p(\mathbf{z}|\mathbf{I})$  where  $\mathbf{I}$  is the observed variable or HSI and  $\mathbf{z}$  is the latent variable,

and a decoder ( $D_\theta$ ) that generates new data  $p(\mathbf{I}|\mathbf{z})$  from samples of the latent code  $\mathbf{z} \sim p(\mathbf{z})$  [22] (Fig. 1). In practice, both the encoder and decoder are neural networks that represent  $q_\psi(\mathbf{z}|\mathbf{I})$  (approximate posterior) and  $p_\theta(\mathbf{I}|\mathbf{z})$ , respectively.  $\psi$  and  $\theta$  represent the variational and generational parameters, respectively, and are jointly learned by maximising the Evidence Lower Bound (ELBO):

$$\mathcal{L}(\theta, \psi, \mathbf{I}^{(i)}) = \mathbb{E}_{q_\psi(\mathbf{z}|\mathbf{I}^{(i)})}[\log p_\theta(\mathbf{I}^{(i)}|\mathbf{z})] - D_{KL}(q_\psi(\mathbf{z}|\mathbf{I}^{(i)})||p_\theta(\mathbf{z})), \quad (1)$$

where  $\mathbf{I}^{(i)}$  is the  $i^{th}$  HSI from the training dataset of size  $S$ . The first term corresponds to the reconstruction error. The second, considered as a regularisation term, allows the approximate posterior distribution  $q_\psi(\mathbf{z}|\mathbf{I})$  to be reconciled with the prior  $p_\theta(\mathbf{z})$  of the model (generally  $p(\mathbf{z}) \sim \mathcal{N}(0, I)$ ). This term is called the Kullback-Liebr (KL) divergence and is used to calculate the distance between two distributions. Training is enabled by the reparameterisation trick, which consists of writing the random variable  $\mathbf{z}$  as a deterministic variable  $\mathbf{z} = \mu + \sigma \cdot \epsilon$ , with  $\epsilon \sim \mathcal{N}(0, 1)$ . The encoder output therefore becomes  $\mu$  and  $\sigma$ . The overall architecture is shown in Fig. 1.

**Convolutional neural network** CNNs are inspired by the visual system [23]. They are based on the weight-share mechanism through convolution filters that slide along the input features. This significantly reduces the number of network parameters compared to fully connected networks. A CNN is typically composed of a convolutional feature extractor followed by task-dependent layers, such as regression or decoding layers. The feature extractor is the convolutional part of the network, and consists of multiple convolution layers. A learnable convolution filter (or kernel) is applied to extract the local descriptors from the input maps. Following the convolution, an activation function is applied in order to improve the non-linearity of the network. A pooling layers then further reduces the size of the resulting feature maps, thus obtaining more general and abstract features. Additional layers may then be used to map the extracted features to task-dependent outputs.

### 3.2 Proposed emulation framework

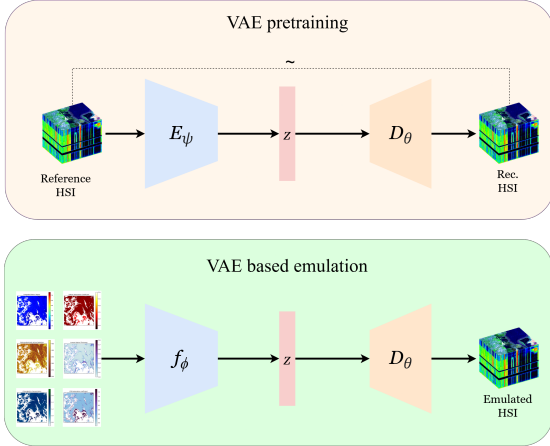


Figure 2: Two-step VAE-based emulation: (top) a VAE is first trained to reproduce hyperspectral images as input. Then, (bottom) an interpolator  $f_\phi$  is trained to link the biophysical parameters to the learned latent space. The one-step formulation consists solely of the bottom part.

Traditionally, HS image emulation is performed in two stages. First, a dimensionality reduction step is applied to the data, typically using principal component analysis (PCA) on the image spectra. Second, a regression model is trained to predict the projection coefficients of new spectra [10]. This framework circumvents the limitations of regression models when applied directly to high-dimensional data such as HSI. As dimensionality reduction is implicit in a variational autoencoder (VAE), we first investigated a more direct formulation, in which a VAE-based model is trained to map the biophysical parameters  $\mathbf{Y}$  to the emulated hyperspectral data  $\hat{\mathbf{I}}$ . Then, we extended the VAE-based framework to include a pretraining step first.

Unlike linear methods, a VAE can capture non-linear relationships both within and across spectral bands, thereby preserving the complexity of hyperspectral signatures [24]. Moreover, its variational formulation constrains the latent space to follow a Gaussian prior, which enables consistent random sam-

pling and ensures that neighboring latent codes decode into spectrally similar outputs [22]. Formally, an encoder network  $f_\phi$  maps the input  $\mathbf{Y}$  into a latent representation  $z$ , from which a decoder  $D_\theta$  generates the emulated data:

$$z \sim f_\phi(\mathbf{Y}) = q_\phi(z|\mathbf{Y}), \quad \hat{\mathbf{I}} \sim D_\theta(z) = p_\theta(\mathbf{I}|z), \quad (2)$$

where  $q_\phi$  denotes a latent mapping induced by the biophysical parameters, and  $p_\theta$  denotes the decoder distribution. For simplicity, we write  $\hat{\mathbf{I}} = D_\theta(f_\phi(\mathbf{Y}))$ .

The parameters  $\phi$  and  $\theta$  are optimized to minimize a reconstruction loss between the emulated images  $\hat{\mathbf{I}}$  and the reference images  $\mathbf{I}$ , with an additional Kullback–Leibler divergence term used to regularize the latent distribution:

$$\min_{\phi, \theta} \mathcal{L}(\theta, \phi, \mathbf{Y}) = \min_{\phi, \theta} \left( \|\mathbf{I} - D_\theta(f_\phi(\mathbf{Y}))\|_2^2 + D_{KL}(q_\phi(z|\mathbf{Y})||p_\theta(z)) \right). \quad (3)$$

While this direct VAE-based formulation is conceptually appealing, it suffers from practical limitations: the encoder must simultaneously learn both the spectral structure of hyperspectral data and their dependency on the biophysical parameters, which can lead to suboptimal reconstructions and limited generalization, especially in a high-dimensional setting. To overcome this, we adopted a two-step approach inspired by traditional emulation frameworks. Figure 2 describes the two steps of the method we propose.

We first train a VAE directly on hyperspectral data  $\mathbf{I}$  to encode them into a latent representation  $z$ , from which the decoder reconstructs the input:

$$z \sim E_\psi(\mathbf{I}) = q_\psi(z|\mathbf{I}), \quad \hat{\mathbf{I}} \sim D_\theta(z) = p_\theta(\mathbf{I}|z), \quad (4)$$

where  $q_\psi$  and  $p_\theta$  denote the approximate posterior and the prior, respectively. Once the VAE is trained and validated for faithful HSI reconstruction, the encoder is discarded. An interpolator  $f_\phi$  is then trained to perform the second phase by linking the biophysical input variables to the latent space, based on Equation 3.

This combined VAE–interpolator approach offers two key advantages. First, the training and validation of each component (VAE for dimensionality reduction and interpolator for parameter mapping) can

Table 1: Summary of the proposed hyperspectral emulation framework variants.

Method	Latent representation	Parameter mapping	Spatial modeling	Training strategy	Output
P2P	No	Direct	No	One-step	Spectra
P2P-pre	Yes (spectra)	Interpolator	No	Two-step	Spectra
FC-VAE	No	Direct	Yes	One-step	HSI
FC-VAE-pre	Yes (HSI)	Interpolator	Yes	Two-step	HSI

be carried out sequentially and independently, which facilitates hyperparameter optimization. Second, the model is highly adaptable: any modification of the biophysical input parameters, without altering the properties of the target HSI, only requires retraining the interpolator, leading to significant computational savings.

### 3.3 Variants

To evaluate the proposed framework, we implemented two emulator families: a simple pixel-to-pixel baseline, denoted as P2P, and a fully convolutional VAE that incorporates spatial information. We denote the latter as FC-VAE. For each family, we trained two versions: a one-step formulation and a two-step formulation denoted by the suffix *-pre*. Table 1 summarizes the different instantiations of the proposed emulation framework and their main characteristics.

**Pixel-to-pixel emulator (P2P).** As a first baseline, we implemented a pixel-to-pixel emulator. The encoder  $E_\psi$ , interpolator  $f_\phi$ , and decoder  $D_\theta$  are all implemented as multilayer perceptrons (MLPs). The structures of  $E_\psi$  and  $f_\phi$  are identical except for the input layer size, while the decoder  $D_\theta$  mirrors this structure in reverse. Since each pixel (spectrum) is processed independently, the emulator focuses in the spectral domain, at the expense of spatial correlations across the scene.

**Fully convolutional VAE (FC-VAE).** In the second family (Figure 2), we adopt a fully convolutional design. Both the encoder  $E_\psi$  and interpolator  $f_\phi$  start with a  $1 \times 1$  pointwise convolution to extract spectral features while preserving spatial resolution. This is followed by convolutional layers ( $7 \times 7$ , and  $3 \times 3 \downarrow$ )

downconvolutional layers, the number of which depends on the tested dataset. Each layer is succeeded by channel normalization. The final feature map is projected into  $\mu$  and  $\log \sigma^2$  through  $1 \times 1$  convolutions, representing the mean and log-variance of the approximate posterior  $q_\psi(\mathbf{z}|\mathbf{I})$ . The decoder  $D_\theta$  mirrors this structure in reverse. For upsampling, we follow the strategy of [25]: a nearest-neighbor upsampling followed by convolution, which mitigates checkerboard artifacts compared to transpose convolutions. Unlike P2P, the FC-VAE directly emulates hyperspectral cubes, thus preserving spatio-spectral coherence.

## 4 Emulation experiments and results

This section evaluates the proposed VAE-based hyperspectral emulation framework under different architectural and training configurations. In particular, we study the impact of pixel-wise versus spatial-spectral modeling, as well as one-step versus two-step (pre-trained) training strategies. Experiments are conducted on both a simulated vegetation dataset and real Sentinel-3 OLCI imagery to assess model behavior under controlled physical simulation as well as real-world observational conditions. The proposed models are compared against classical regression-based emulators and machine learning baselines commonly used in hyperspectral emulation. We report reconstruction accuracy, spectral fidelity and runtime performance on CPU/GPU.

### 4.1 Datasets

We evaluate the proposed framework on two complementary datasets: a simulated vegetation dataset generated with PROSAIL, and real Sentinel-3 OLCI

ocean colour imagery. Detailed descriptions of the simulated PROSAIL dataset generation, parameterization, and composition are provided in a separate data publication [26].

**Sentinel-3 Ocean Colour** Sentinel-3 carries multiple instruments, including the Ocean and Land Colour Instrument (OLCI), a pushbroom imaging spectrometer that acquires radiance measurements in 21 bands spanning the visible (VIS) to near-infrared (NIR) range at a spatial resolution of 300 m. The Sentinel-3 OLCI Ocean Colour dataset used in this study consists of radiance images (21 spectral bands, Level-1 products) [27], together with atmospherically corrected reflectances and associated biophysical parameters related to ocean colour (Level-2 products) [28]. Among the latter, six independent variables were selected as emulator inputs: chlorophyll-a concentration (Chl), total suspended matter concentration (TSM), diffuse attenuation coefficient (Kd), photosynthetically active radiation (PAR), aerosol Ångström exponent ( $\text{\AA}$ ), and integrated water vapour (IWV) [29].

The dataset comprises OLCI acquisitions over several oceanic regions. Each image was cropped into patches of size  $128 \times 128$ , and only patches dominated by water pixels were retained, with at least 40% of pixels labeled as water and at most 20% of pixels belonging to other classes (cloud, land, snow, ice). This filtering resulted in a total of 100 000 input–output pairs suitable for training and evaluation.

**Simulated PROSAIL dataset** The second dataset consists of  $64 \times 64 \times 211$  hyperspectral images with their corresponding bio-optical parameter maps generated by the PROSAIL model [3]. PROSAIL combines the PROSPECT leaf optical properties model [4] and the SAIL canopy bidirectional reflectance model [5], extended with an additional soil bidirectional reflectance distribution function (BRDF) to provide realistic soil reflectance  $\rho_c$ . We use the PROSPECT-D version which accounts for the contribution of brown pigments. At the leaf level, PROSPECT-D is driven by leaf structure, pigment contents (chlorophyll, carotenoids, anthocyanins, and brown pigments), equivalent water thickness, and dry

matter content. At the canopy level, SAIL requires parameters describing vegetation structure and viewing geometry, including leaf area index, leaf angle distribution, hotspot effects, and illumination and observation angles. Soil spectra are supplied for each selected region under the assumption of within-region homogeneity, and are drawn from the ICRAF-ISRIC soil spectral library [30].

To construct the simulated dataset, Sentinel-2 multispectral images are first inverted using look-up tables (LUTs) generated with PROSAIL to obtain spatial maps of the bio-optical parameters. These parameter maps provide realistic spatial distributions across the scene and are subsequently used to drive forward PROSAIL simulations, producing pixel-wise canopy reflectance spectra that are rearranged to form hyperspectral cubes. The resulting dataset consists of 11,140 hyperspectral cubes spanning multiple geographic regions, with a ground sampling distance (GSD) of 20 m. These were divided into training, validation, and test subsets.

## 4.2 Implementation details

For each dataset, model architectures and training parameters were adapted to the number of spectral bands and the dimensionality of the data. For the Sentinel-3 dataset, fully convolutional models are trained on spatial patches, whereas pixel-wise models operate at the spectral level. For the simulated PROSAIL dataset, convolutional models are trained on full hyperspectral cubes, while pixel-wise models are trained using individual spectra extracted from the same scenes.

For the Sentinel-3 dataset, hyperspectral patches are split into training and validation subsets, with 25000 samples used for training and 5000 samples for validation in the FC-VAE implementations. Pixel-wise (P2P) models are trained and validated using approximately 160000 individual spectra extracted from the same dataset, while an independent set of 2500 hyperspectral cubes is reserved for testing. For the simulated PROSAIL dataset, the 11140 hyperspectral cubes are divided into training (70%), validation (20%), and test (10%) subsets. Convolutional models are trained on the full training split, whereas pixel-

wise models are trained at the spectral level using approximately 3000 individual spectra.

For the FC-VAE variants, convolutional layers widths are set to 40–80–160–320–640 for the Sentinel-3 dataset and to 400–600–800 for the simulated dataset, with a latent dimension fixed to  $z = 20$  in all cases. For the pixel-wise implementations, multilayer perceptrons with hidden layer sizes of 256 and 512 are used, again with a latent dimension of  $z = 20$ .

To mitigate KL divergence vanishing during VAE training, a cyclic annealing strategy is employed, with a maximum KL weight of  $10^{-3}$ . The annealing period is set to 15 epochs for FC-VAE models and 50 epochs for P2P models. All models are trained using an initial learning rate of  $10^{-4}$ , decreasing exponentially over 35 epochs before being reset to its initial value. For convolutional architectures, a curriculum learning strategy is adopted to stabilize training. Models are first trained on cropped patches of size  $8 \times 8$ , and the spatial resolution is gradually increased every 100 epochs up to a maximum patch size of  $128 \times 128$  after 400 epochs. This strategy is applied both during VAE pretraining and during the training of the latent-space interpolator in the two-step formulation.

Based on this experimental setup, we now compare our approach against representative baseline methods.

### 4.3 Compared methods

We compare the proposed emulation framework against representative regression-based emulators. As classical reference methods, we consider the Kernel Ridge Regression (KRR) and Gaussian Process Regression (GPR) [10]. These methods follow the two-step emulation framework introduced in previous work. In this setting, principal component analysis (PCA) is first applied to the target spectra to reduce dimensionality, and a regression model is then trained to predict the corresponding principal components from the biophysical input variables. We retain 2 principal components, explaining approximately 99.5% of the spectral variance. Due to computational constraints, these models are trained on progressively larger subsets of the data (from 100 to 3000), and the configuration yielding the lowest validation error is retained.

In addition to these classical approaches, we include a multilayer perceptron (MLP) baseline that directly maps the biophysical input parameters to the full hyperspectral spectrum without explicit dimensionality reduction, using hidden layer sizes of 256 and 512 for both datasets. The MLP uses the same input variables as the other baselines and is trained using the same optimization settings as the pixel-wise implementations of the proposed framework. This baseline serves to assess the benefit of variational and latent-space modeling compared to a standard feedforward regression approach.

All baselines operate at the spectral level and do not explicitly model spatial context. This ensures a fair comparison with the pixel-wise variants of the proposed framework, and highlights the additional benefits of spatial-spectral modeling enabled by the convolutional architectures.

### 4.4 Evaluation metrics

To assess the performance of the proposed framework, we evaluate reconstruction quality and computational efficiency using complementary metrics. These metrics capture global accuracy, spatial structures preservation, spectral fidelity, and perceptual image quality.

Reconstruction accuracy is quantified using the Root Mean Squared Error (RMSE), which provides a global measure of emulation accuracy, with lower values indicating better performance. RMSE is defined as

$$\text{RMSE} = \sqrt{\frac{1}{N \cdot B} \sum_{i=1}^N \sum_{b=1}^B \left( \mathbf{I}_b^{(i)} - \hat{\mathbf{I}}_b^{(i)} \right)^2},$$

where  $\mathbf{I}_b^{(i)}$  and  $\hat{\mathbf{I}}_b^{(i)}$  denote the reference and emulated values at band  $b$  for sample  $i$ ,  $N$  is the number of samples, and  $B$  is the number of spectral bands.

Spatial reconstruction quality is evaluated using the Structural Similarity Index Measure (SSIM) [31], which compares luminance, contrast, and structural information between reference and emulated images, with higher values indicating better spatial agreement.

$$\text{SSIM}(x, y) = \frac{(2\mu_x\mu_y + C_1)(2\sigma_{xy} + C_2)}{(\mu_x^2 + \mu_y^2 + C_1)(\sigma_x^2 + \sigma_y^2 + C_2)},$$

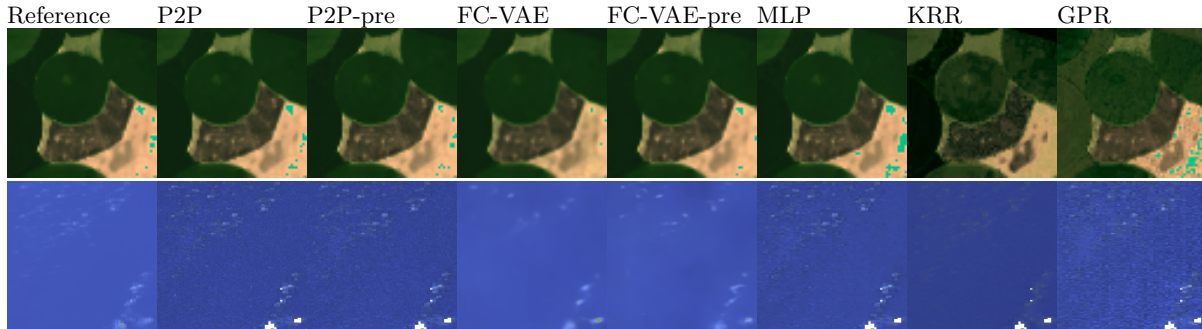


Figure 3: Examples of emulated HSI. Top: Simulated dataset, bottom : Sentinel 3.

where  $\mu_x$ ,  $\mu_y$ ,  $\sigma_x^2$ ,  $\sigma_y^2$ , and  $\sigma_{xy}$  denote the local means, variances, and covariance of images  $x$  and  $y$ , respectively.

Spectral fidelity is assessed using the Spectral Angle (SA) [32], which measures the angular difference between reference and emulated spectra, and is not sensitive to overall magnitude differences. The spectral angle is defined as

$$\text{SA}(\mathbf{I}, \hat{\mathbf{I}}) = \arccos \left( \frac{\langle \mathbf{I}, \hat{\mathbf{I}} \rangle}{\|\mathbf{I}\| \|\hat{\mathbf{I}}\|} \right),$$

where lower values indicate better spectral agreement.

In addition, perceptual reconstruction quality is evaluated using the Peak Signal-to-Noise Ratio (PSNR), defined as

$$\text{PSNR} = 10 \cdot \log_{10} \left( \frac{\text{MAX}^2}{\text{MSE}} \right),$$

where MAX is the maximum possible pixel intensity, and MSE the mean squared error. Higher PSNR values indicate better reconstruction.

Finally, computational efficiency is assessed by measuring inference throughput on CPU and GPU architectures, expressed as the number of hyperspectral images generated per second.

## 4.5 Results

**Results on the simulated dataset** The results on the simulated vegetation dataset are reported in Table 2. Pixel-to-pixel models achieve the strongest overall performance in this setting, consistently producing

the lowest reconstruction errors and highest image quality across all evaluation metrics. The pretrained variant, P2P-pre, shows very similar performance, with slightly degraded reconstruction metrics, indicating limited benefits of pretraining for pixel-to-pixel architectures on this dataset. The MLP achieves comparable reconstruction quality, with RMSE and SSIM close to those of P2P, while exhibiting a slightly higher spectral angle, which suggests a modest degradation in spectral fidelity despite similar spatial reconstruction quality. By contrast, convolutional architectures (FC-VAE and FC-VAE-pre) exhibit higher errors and reduced spectral fidelity, while classical regression-based methods (KRR and GPR) yield the weakest overall performance.

Qualitative results further support these quantitative observations by illustrating the high spatial fidelity achieved by pixel-to-pixel models. As shown in Figure 3, P2P and P2P-pre emulated vegetation scenes are visually indistinguishable from the reference images, with no noticeable spatial artifacts or loss of fine-scale structures.

Spectral fidelity is further examined through comparison of emulated and reference spectra for the best performing model of each family, namely P2P, FC-VAE-pre, and MLP. Figure 4 shows density scatter plots for three representative spectral bands (Green, NIR and SWIR), where perfect spectral agreement would correspond to points lying along the diagonal. On the simulated dataset, all three models show very strong correlation with the reference spectra ( $r > 0.99$ ) with limited dispersion on all bands. P2P reaches a

Table 2: Comparison of the evaluated metrics on the simulated dataset. For reference, a LUT-based emulation generates 0.89 images/s, while the full simulator produces one image every 5.58 seconds. Our models significantly outperform these computation times while maintaining high spectral and spatial fidelity.

	RMSE ( $10^{-2}$ ) ↓	SSIM ↑	PSNR (dB) ↑	SA ( $10^{-2}$ ) ↓	CPU ↑ (images/s)	GPU ↑ (100 images/s)
P2P	<b>0.12</b>	<b>0.9996</b>	<b>49.83</b>	<b>0.44</b>	13.78	55.11
P2P-pre	0.13	0.9995	49.09	0.50	14.35	69.34
FC-VAE	0.55	0.9956	37.39	1.83	0.55	3.78
FC-VAE-pre	0.35	0.9977	41.08	1.29	0.55	3.78
MLP	0.13	0.9994	49.04	0.53	35.37	<b>124.73</b>
KRR	3.8	0.8154	19.80	4.62	<b>254.64</b>	-
GPR	1.05	0.9627	32.81	3.14	11.75	-

perfect correlation, while FC-VAE-pre shows slightly lower correlation coefficient and marginally higher dispersion, consistent with its weaker quantitative performance on this dataset.

**Results on the real-world dataset** Results on the Sentinel-3 OLCI dataset are reported in Table 3. In contrast to the simulated vegetation case, convolutional variational models achieve the strongest overall performance on real-world imagery. In particular, FC-VAE-pre outperforms all other methods across most evaluation metrics, achieving the lowest reconstruction error and the highest perceptual and spatial quality. The non-pretrained FC-VAE performs well but remains systematically behind its pretrained counterpart, highlighting the benefit of pretraining for convolutional architectures on real data. Pixel-to-pixel models, by contrast, exhibit substantially higher reconstruction errors and weaker spectral fidelity, although they remain competitive in terms of SSIM. The MLP achieves intermediate performance, improving upon classical regression-based methods but remaining less accurate than FC-VAE-pre across most metrics.

Qualitative results provide additional support for these results. As shown in Fig. 3, pixel-to-pixel emulations on Sentinel-3 imagery exhibit noticeable noise and local inconsistencies, whereas FC-VAE-pre produces smoother and more spatially coherent reconstructions. In addition, convolutional models are able to exploit spatial context to plausibly inpaint missing

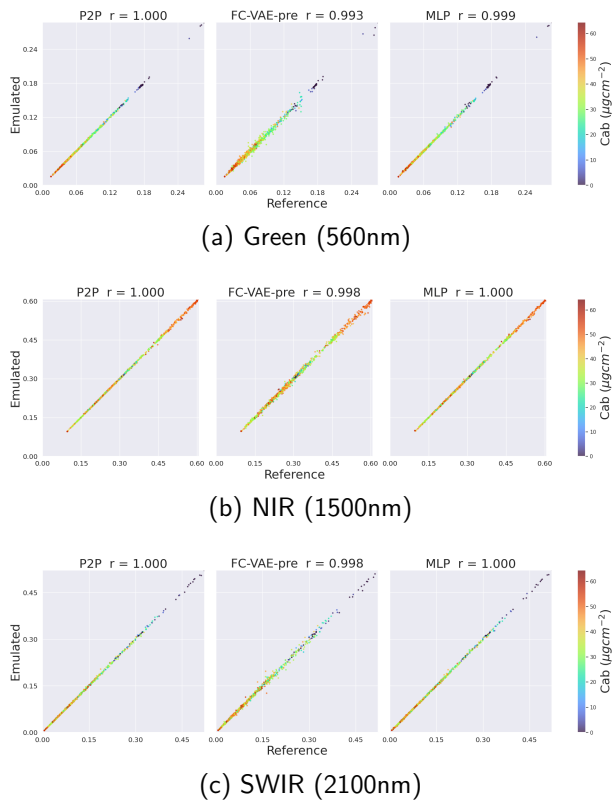


Figure 4: Comparison between emulated and reference values of the given wavelengths on the simulated dataset.

Table 3: Comparison of studied metrics on the Sentinel 3 dataset

	RMSE ↓	SSIM ↑	PSNR (dB)↑	SA ( $10^{-2}$ ) ↓	CPU ↑ (images/s)	GPU ↑ (100 images/s)
P2P	10.32	0.8152	26.83	5.22	7.68	14.32
P2P-pre	10.40	0.8199	26.74	5.10	7.68	15.46
FC-VAE	6.05	0.8938	33.78	3.73	2.11	5.31
FC-VAE-pre	<b>3.68</b>	<b>0.9257</b>	<b>34.36</b>	<b>3.09</b>	2.11	5.15
MLP	9.97	0.8642	27.63	4.65	15.67	<b>36.79</b>
KRR	15.30	0.7708	22.42	10.44	<b>110.57</b>	-
GPR	12.32	0.7794	25.80	7.30	0.01	-

regions, such as land or cloud-contaminated pixels, which contributes to their improved perceptual quality.

Using the same density scatter plot analysis as above, Figure 5 compares emulated and reference spectra for the Sentinel-3 dataset across three representative bands (Green, Red, and NIR). All models exhibit strong correlations with the reference spectra, although pixel-to-pixel models display increased dispersion. FC-VAE-pre shows slightly lower correlation coefficients but reduced dispersion, consistent with its improved robustness on real-world data.

**Cross-dataset interpretation** Taken together, the results reveal a clear dataset-dependent behavior: the models that performs best on simulated data are not necessarily those that perform best on real satellite imagery. On the simulated vegetation dataset, pixel-to-pixel models achieve the highest reconstruction accuracy because the data are generated spectrum-wise under controlled physical assumptions, with smooth parameter fields, limited noise, and strong spectral consistency. In this context, emulators primarily act as fast surrogates of forward models, and explicit spatial modeling provides limited additional benefit.

In contrast, real Sentinel-3 imagery is characterized by spatial heterogeneity, sensor noise, and missing or contaminated pixels, which make purely pixel-wise emulation less robust. Under these conditions, accounting for spatial context becomes essential. Convolutional variational models better handle spatial variability by producing more spatially consistent re-

constructions and plausibly inpaint missing regions, as observed in the qualitative results, leading to im-

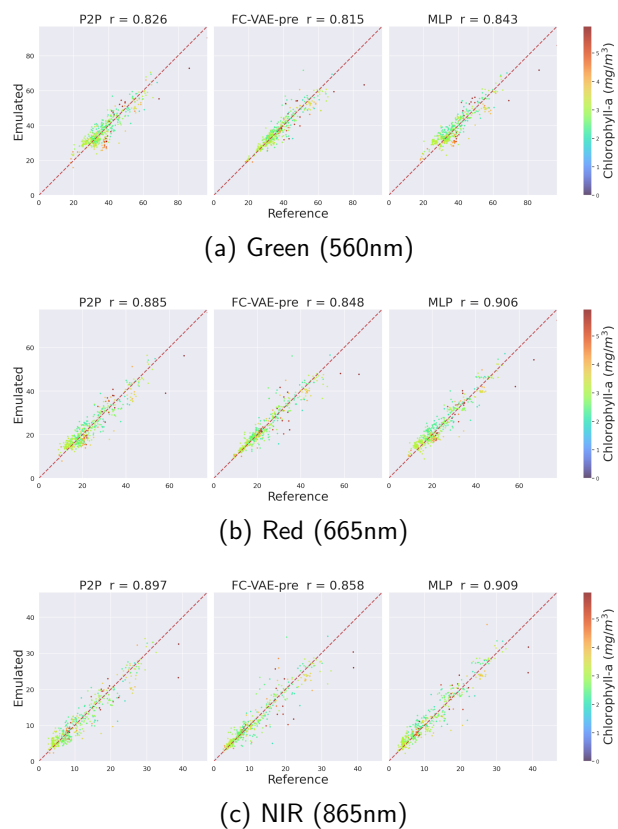


Figure 5: Sentinel 3 dataset scatter plots : comparison between emulated and reference values of the given wavelengths.

proved robustness on real-world data.

More generally, these observations indicate that pixel-to-pixel emulation remains well-suited to purely simulated settings, but becomes insufficient once real observational effects are introduced. Emulator design should therefore be guided by the characteristics of the target data and the intended use case, rather than by performance on simulated benchmarks alone. There is no universally optimal architecture: pixel-wise emulators are well suited to controlled simulation-based workflows, whereas spatial-spectral models are better adapted to real-world observational data.

**Computational efficiency** Computational efficiency is summarized in Tables 2 and 3 in terms of inference throughput on CPU (AMD EPYC 7643, 16 cores) and GPU (Nvidia A100 40GB) architectures, expressed as the number of hyperspectral images generated per second.

Classical regression methods, in particular KRR, achieve the highest throughput on CPU, but at the cost of substantially lower reconstruction accuracy. Among learning-based approaches, the MLP is the most efficient on GPU, providing high throughput while maintaining competitive performance relative to pixel-wise and convolutional models. Convolutional variational models exhibit lower throughput due to their increased architectural complexity. Nevertheless, this reduced throughput is accompanied by improved robustness and reconstruction quality on real-world data.

Overall, these results illustrate the expected trade-off between accuracy and efficiency and highlight that computational considerations should be weighed alongside data characteristics when selecting an emulation strategy.

## 5 Use case for emulated datasets: Practical evaluation

**Motivation** The results presented in Section 4 demonstrate that the proposed emulation models are

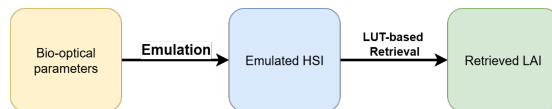


Figure 6: Experimental setup: First, a hyperspectral image is generated using an emulation model. Then we apply LUT-based inversion to retrieve the *Leaf Area Index* estimation from the image.

able to reproduce hyperspectral data with high spectral and spatial fidelity. However, reconstruction accuracy alone does not necessarily guarantee that emulated data are suitable for practical remote sensing applications. In particular, small spectral or spatial discrepancies may be propagated when emulated hyperspectral images are used as inputs to nonlinear inversion or retrieval algorithms. To assess the practical reliability of the proposed emulation framework, we therefore evaluate its impact on a representative downstream task, namely the retrieval of biophysical parameters using a look-up table (LUT)-based inversion approach.

**Experimental setup** To evaluate the impact of emulated hyperspectral data on downstream biophysical parameter retrieval, we consider a LUT-based inversion for *Chlorophyll a+b* ( $C_{ab}$ ) estimation. The LUTs are generated from simulated PROSAIL data and are applied to hyperspectral emulated images using different models, namely P2P, FC-VAE-pre, MLP, and GPR models. The resulting  $C_{ab}$  maps are compared to reference  $C_{ab}$  obtained from the original hyperspectral simulated data. Figure 6 illustrates the overall experimental process.

### Results on biophysical parameter retrieval

Figure 7 reports the relative errors of *Chlorophyll a+b* ( $C_{ab}$ ) retrieval obtained from hyperspectral emulated images using different models. The P2P emulator achieves the lowest relative error (0.28%), followed by the MLP (0.35%) and the FC-VAE-pre (0.50%). All these three methods show similar error spatial distribution, with higher errors mainly concentrated in transition areas between vegetation parcels, while

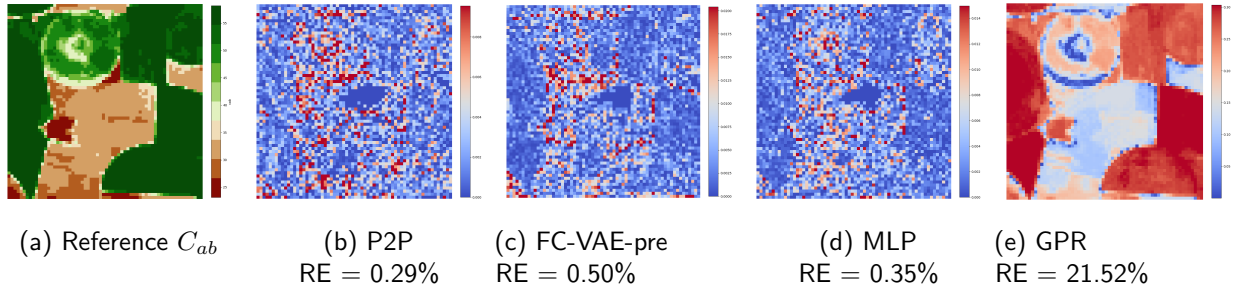


Figure 7: Pixel-wise normalized mean absolute error (Relative error, RE) (%) between reference  $C_{ab}$  retrieved on simulated data (a) and  $C_{ab}$  retrieved on P2P (b), FC-VAE-pre (c), MLP (d), and GPR (e) emulated scenes.

interior regions remain accurately reconstructed. By contrast, the GPR-based emulation yields substantially larger errors (21.52%), with pronounced artifacts and a clear degradation of retrieval accuracy in regions with high  $C_{ab}$  values. These results indicate that, while several learning-based emulators preserve retrieval performance to a similar extent, classical regression-based approaches may introduce distortions that significantly impact nonlinear inversion outcomes.

#### Implications for practical use of emulated data

These results highlight that high reconstruction accuracy does not automatically translate into reliable performance in downstream applications, and that the choice of an emulation strategy can have a significant impact on inversion outcomes. Pixel-wise and latent space learning-based emulators preserve biophysical parameter retrieval accuracy within a narrow margin relative to reference simulations, whereas classical regression-based approaches may introduce spatially structured errors, amplified by the nonlinear inversion. This observation underscores the importance of evaluating hyperspectral emulators not only in terms of spectral or spatial fidelity, but also with respect to their behavior in representative end-use scenarios.

## 6 Summary and discussion

**Architecture-dependent behavior** First, the choice of architecture strongly depends on the application domain. Pixel-to-pixel (P2P) models achieve the highest fidelity on simulated vegetation data, with strong preservation of spectral signatures. Several factors may explain this behavior: (i) the dimensionality reduction is less severe, limiting information loss; (ii) representing independent spectra in a compact latent space is simpler than encoding full hyperspectral cubes; and (iii) learning local spectral dependencies is inherently easier in the case of isolated spectra. These properties collectively account for the superior performance of P2P approaches on simulated vegetation data.

By contrast, Sentinel-3 data exhibit greater homogeneity across scenes. In this setting, pixel-to-pixel emulation tends to produce noisier reconstructions. Fully convolutional VAEs, particularly when pretrained, perform better by explicitly modeling spatio-spectral correlations, thereby yielding smoother and more coherent outputs. They can also inpaint missing regions, such as land and cloud pixels.

**Training strategy insights** Second, pretraining proves beneficial in convolutional settings, improving both reconstruction accuracy and training stability. However, for P2P emulators, pretraining provides limited gains, as convergence is already fast, suggesting

that the added complexity is unnecessary when spatial correlations are not explicitly modeled.

**Practical implications and limitations** Third, our evaluation against classical regression-based emulators highlights differences in both accuracy and robustness. While methods such as KRR and GPR remain competitive in CPU-limited scenarios, they consistently underperform in terms of reconstruction accuracy. By contrast, the proposed VAE-based framework offers a favorable trade-off between accuracy and computational efficiency, particularly when executed on GPU architectures.

In addition, the practical usability of the emulated data was assessed through a downstream application, namely LUT-based retrieval of *Chlorophyll a+b* ( $C_{ab}$ ). Pixel-to-pixel emulators achieved the best retrieval performance, closely followed by the MLP. These results highlight the potential of emulated hyperspectral data for downstream applications, while also underscoring the need for careful evaluation of model-induced biases when emulation outputs are used in nonlinear inversion workflows.

## 7 Conclusion and perspectives

In this work, we proposed a VAE-based framework for hyperspectral image emulation, exploring both direct one-step and two-step formulations across pixel-to-pixel and fully convolutional variants. Through experiments on simulated PROSAIL data and real Sentinel-3 OLCI imagery, we showed that the choice of emulation strategy should be guided by the characteristics of the target data. Pixel-to-pixel models are best suited to controlled simulation settings, where they achieve high spectral fidelity, whereas fully convolutional VAEs are more effective on real-world observations by leveraging spatial context to better handle spatial heterogeneity and missing or contaminated pixels.

Moving forward, future work will focus on the estimation and characterization of model-induced uncertainties associated with the proposed emulation framework, as well as on the analysis of their propagation in downstream applications. In a second stage,

we will investigate alternative generative modeling approaches, such as diffusion models and normalizing flows, to explore how different generative formulations impact reconstruction accuracy, computational cost, and uncertainty behavior in hyperspectral emulation.

## Acknowledgment

This work is partially funded by the ULCO research pole “Mutations Technologiques et Environnementales”, EUR MAIA (ANR-22-EXES-0009), and Hauts-de-France region. This work is supported by the graduate school IFSEA that benefits from a France 2030 grant (ANR-21-EXES-0011) operated by the French National Research Agency. Experiments presented in this paper were carried out using the CALCULCO computing platform, supported by DSI/ULCO (Direction des Systèmes d’Information de l’Université du Littoral Côte d’Opale).

## References

- [1] M. Govender, K. Chetty, and H. Bulcock, “A review of hyperspectral remote sensing and its application in vegetation and water resource studies,” *Water SA*, vol. 33, no. 2, Dec. 2009. [Online]. Available: <https://www.ajol.info/index.php/wsa/article/view/49049>
- [2] P. Ghamisi, N. Yokoya, J. Li, W. Liao, S. Liu, J. Plaza, B. Rasti, and A. Plaza, “Advances in hyperspectral image and signal processing: A comprehensive overview of the state of the art,” *IEEE Geoscience and Remote Sensing Magazine*, vol. 5, no. 4, pp. 37–78, 2017.
- [3] S. Jacquemoud, W. Verhoef, F. Baret, C. Bacour, P. J. Zarco-Tejada, G. P. Asner, C. François, and S. L. Ustin, “Prospect+sail models: A review of use for vegetation characterization,” *Remote Sensing of Environment*, vol. 113, pp. S56–S66, 2009, imaging Spectroscopy Special Issue.
- [4] S. Jacquemoud and F. Baret, “Prospect: A model of leaf optical properties spectra,” *Remote sens-*

- ing of environment, vol. 34, no. 2, pp. 75–91, 1990.
- [5] W. Verhoef, “Light scattering by leaf layers with application to canopy reflectance modeling: The sail model,” *Remote sensing of environment*, vol. 16, no. 2, pp. 125–141, 1984.
- [6] C. Guilloteau, T. Oberlin, O. Berné, and N. Dobigeon, “Hyperspectral and multispectral image fusion under spectrally varying spatial blurs—application to high dimensional infrared astronomical imaging,” *IEEE Trans. Comput. Imaging*, vol. 6, pp. 1362–1374, 2020.
- [7] S. Yu, W. Hannah, L. Peng, J. Lin, M. A. Bhouri, R. Gupta, B. Lütjens, J. C. Will, G. Behrens, J. Busecke *et al.*, “Climsim: A large multi-scale dataset for hybrid physics-ml climate emulation,” *Advances in neural information processing systems*, vol. 36, pp. 22 070–22 084, 2023.
- [8] C. Ben Azizi, C. Guilloteau, G. Roussel, and M. Puigt, “Coupled VAE and interpolator approach for fast hyperspectral image emulation,” in *2024 14th Workshop on Hyperspectral Imaging and Signal Processing: Evolution in Remote Sensing (WHISPERS)*. IEEE, 2024, pp. 1–5.
- [9] J. Verrelst, M. Morata, J. L. García-Soria, Y. Sun, J. Qi, and J. P. Rivera-Caicedo, “Rtm surrogate modeling in optical remote sensing: A review of emulation for vegetation and atmosphere applications,” *Remote Sensing*, vol. 17, no. 21, 2025. [Online]. Available: <https://www.mdpi.com/2072-4292/17/21/3618>
- [10] J. Verrelst, J. P. Rivera Caicedo, J. Muñoz-Marí, G. Camps-Valls, and J. Moreno, “Scope-based emulators for fast generation of synthetic canopy reflectance and sun-induced fluorescence spectra,” *Remote Sensing*, vol. 9, no. 9, p. 927, 2017.
- [11] J. Verrelst, J. P. Rivera Caicedo, J. Vicent, P. Morcillo Pallarés, and J. Moreno, “Approximating empirical surface reflectance data through emulation: opportunities for synthetic scene generation,” *Remote sensing*, vol. 11, no. 2, p. 157, 2019.
- [12] M. Morata, B. Siegmann, P. Morcillo-Pallarés, J. P. Rivera-Caicedo, and J. Verrelst, “Emulation of sun-induced fluorescence from radiance data recorded by the hyplant airborne imaging spectrometer,” *Remote sensing*, vol. 13, no. 21, p. 4368, 2021.
- [13] V. Laparra, J. Malo, and G. Camps-Valls, “Dimensionality reduction via regression in hyperspectral imagery,” *IEEE J. Sel. Topics in Signal Processing*, vol. 9, no. 6, pp. 1026–1036, 2015.
- [14] K. Duffy, T. Vandal, W. Wang, R. Nemani, and A. R. Ganguly, “Deep learning emulation of multi-angle implementation of atmospheric correction (maiac),” *arXiv preprint arXiv:1910.13408*, 2019.
- [15] S. Ojaghi, Y. Bouroubi, S. Foucher, M. Bergeron, and C. Seynat, “Deep learning-based emulation of radiative transfer models for top-of-atmosphere brdf modelling using sentinel-3 olci,” *Remote Sensing*, vol. 15, no. 3, 2023. [Online]. Available: <https://www.mdpi.com/2072-4292/15/3/835>
- [16] A. E. Jasso-Garduño, I. Muñoz-Máximo, D. Pinto, and J. M. Ramírez-Cortés, “Deep learning based emulation of radiative transfer code for atmospheric correction of satellite images,” *Computación y Sistemas*, vol. 28, no. 4, pp. 2327–2341, 2024.
- [17] W. Liu, J. You, and J. Lee, “Hsigan: A conditional hyperspectral image synthesis method with auxiliary classifier,” *IEEE Journal of Selected Topics in Applied Earth Observations and Remote Sensing*, vol. 14, pp. 3330–3344, 2021.
- [18] B. Palsson, M. O. Ulfarsson, and J. R. Sveinsson, “Synthesis of synthetic hyperspectral images with controllable spectral variability using a generative adversarial network,” *Remote Sensing*, vol. 15, no. 16, p. 3919, 2023.
- [19] Y. Shi, L. Han, L. Han, S. Chang, T. Hu, and D. Dancy, “A latent encoder coupled generative adversarial network (le-gan) for efficient hyperspectral image super-resolution,” *IEEE Trans. Geosci. Remote Sens.*, vol. 60, pp. 1–19, 2022.

- [20] F. Hadi, J. Yang, M. Ullah, I. Ahmad, G. Farooque, and L. Xiao, "Dhcae: Deep hybrid convolutional autoencoder approach for robust supervised hyperspectral unmixing," *Remote Sensing*, vol. 14, no. 18, p. 4433, 2022.
- [21] R. A. Borsoi, T. Imbiriba, J. C. M. Bermudez, and C. Richard, "Deep generative models for library augmentation in multiple endmember spectral mixture analysis," *IEEE Geosci. Remote Sens. Lett.*, vol. 18, no. 10, pp. 1831–1835, 2020.
- [22] D. P. Kingma and M. Welling, "Auto-encoding variational bayes," *arXiv preprint arXiv:1312.6114*, 2013.
- [23] K. He, X. Zhang, S. Ren, and J. Sun, "Deep residual learning for image recognition," in *Proc. IEEE CVPR*, 2016, pp. 770–778.
- [24] A. Zare and K. Ho, "Endmember variability in hyperspectral analysis: Addressing spectral variability during spectral unmixing," *IEEE Signal Process. Mag.*, vol. 31, no. 1, pp. 95–104, 2014.
- [25] A. Odena, V. Dumoulin, and C. Olah, "Deconvolution and checkerboard artifacts," *Distill*, 2016. [Online]. Available: <http://distill.pub/2016/deconv-checkerboard>
- [26] C. Ben Azizi, C. Guilloteau, G. Roussel, and M. Puigt, "Svh-bd: Synthetic vegetation hyperspectral benchmark dataset for emulation of remote sensing images," 2026, manuscript submitted to Data in Brief.
- [27] L. Bourg, A. Mangin, and O. F. d'Andon, "OLCI Level 0, Level 1b Algorithm Theoretical Basis Document," Thales Alenia Space, Tech. Rep. S3-ACR-TN-007, 10 2014.
- [28] R. Doerffer, "OLCI level 2 algorithm theoretical basis document ocean colour turbid water," ESA technical report, available online at [https://step.esa.int/docs/extra/OLCILL2\\_ATBD\\_Ocean.Colour.Turbid.Water.pdf](https://step.esa.int/docs/extra/OLCILL2_ATBD_Ocean.Colour.Turbid.Water.pdf), 2009.
- [29] C. Donlon, B. Berruti, A. Buongiorno, M.-H. Ferreira, P. Féménias, J. Frerick, P. Goryl, U. Klein, H. Laur, C. Mavrocordatos *et al.*, "The global monitoring for environment and security (gmes) sentinel-3 mission," *Remote sensing of Environment*, vol. 120, pp. 37–57, 2012.
- [30] W. A. (ICRAF), I. S. Reference, and I. C. (ISRIC), "ICRAF-ISRIC Soil VNIR Spectral Library," 2021, dataset. [Online]. Available: <https://doi.org/10.34725/DVN/MFHA9C>
- [31] Z. Wang, A. C. Bovik, H. R. Sheikh, and E. P. Simoncelli, "Image quality assessment: from error visibility to structural similarity," *IEEE Trans. Image Process.*, vol. 13, no. 4, pp. 600–612, 2004.
- [32] R. H. Yuhas, A. F. Goetz, and J. W. Boardman, "Discrimination among semi-arid landscape endmembers using the spectral angle mapper (SAM) algorithm," in *JPL, Summaries of the Third Annual JPL Airborne Geoscience Workshop. Volume 1: AVIRIS Workshop*, 1992.